Satellite valleys and strained band gap transition of bulk Ge: Impact of pseudopotential approximations on quasiparticle levels

Satellite valleys and strained band gap transition of bulk Ge: Impact of pseudopotential approximations on quasiparticle levels

G. Greene-Diniz* and J. C. Abreu and M. Grüning
Atomistic Simulation Centre, Queens University Belfast, Belfast BT7 1NN, Northern Ireland, United Kingdom
(Dated: February 26, 2018)

A first principles study of the electronic structure of strained Ge is carried out within the framework of plane wave pseudopotential density functional theory (DFT) combined with the GW approximation to the self-energy. Systematic investigations of the variations of high symmetry quasiparticle gaps over for a range of pseudopotential approximations are carried out. It is found that the quasiparticle corrections can be at least as sensitive to the choice of DFT approximation as to pseudopotential generation scheme, level of core-valence interaction, and pseudopotential electronic configuration. The latter can be decisive in the resulting prediction of the band gap transition strain, as the magnitudes of exchange and correlation terms involved in the quasiparticle corrections at the conduction valleys are largely determined by the arrangement of orbitals at those regions of the bandstructure, which in turn is determined by the pseudized electronic configuration.

I. INTRODUCTION

Progress in computing technology largely relies on the concomitant increases in performance and energy efficiency of Complimentary Metal Oxide Semiconductor (CMOS) devices, which has motivated the study of high carrier mobility materials. Bulk Ge has attracted a large proportion of these studies. While the well known issues associated with the native oxides form a major reason for the wide spread use of Si in the CMOS device industry,[1] the higher electron and hole mobility in Ge[2,3] make it an attractive material for applications in novel nanoscale devices such as tunnel field effect transistors.[4] In addition, a strain induced transition to a direct band gap in Ge indicates the possibility of optical electronics applications.[5] This is currently driving the use of strained Ge in the development of integrated photonic devices compatible with a conventional Si platform, paving the way for high-speed, energy efficient optical components coexisting with electronic devices on the same chip.[6–8] Thus, there are significant technological imperatives to understand the precise nature of the electronic structure of strained Ge, particularly the electronic bands involved in the technologically relevant optical transitions.

In the absence of strain, Ge is an indirect gap semiconductor. Recently, experimental photoluminescence (PL) studies show a sharp increase in the PL spectra associated with direct electron-hole transitions when sufficient biaxial strain in the (100) plane is applied, indicating a transition to a direct band gap in Ge, with the conduction band minimum (CBM) at the Γ point.[9] However, a review of the reported values of (100) biaxial strain ε_{dir}^{biax} required to achieve a direct band gap in bulk Ge—as predicted from empirical simulations and extracted from experiments—varies over the range ∼1.7-2.0%.[10–14] Experimental techniques to determine strain magnitude can disagree by ∼0.3% when the Ge film sample reaches bulk-like thickness (> 200 nm).[14] Such spreads in data often motivate calculations using first principles methods. In particular, density functional theory (DFT)[15–18] represents arguably the most popular and successful method for calculating properties of solid state materials relevant to technology from first principles. Within the Kohn-Sham (KS) framework, DFT[19] replaces the many body problem of interacting electrons with noninteracting fermions moving in an effective mean field potential (with the condition that the noninteracting system reproduces the electron density of the interacting one). Though in principle DFT is a ground state theory, it is commonly used to estimate the quasiparticle energies and band gaps from the KS bandstructure. The band gaps resulting from KS-DFT calculations however are systematically underestimated,[20–22] and the state-of-the-art to obtain quasiparticle energies and band gaps from first principles relies on the DFT+GW approach. In the latter approach, based on Green's function many-body perturbation theory,[23] the KS bandstructure is perturbatively corrected to the first order within the so-called GW approximation. First principles atomistic simulations based on DFT(+GW) thus can complement experiments and help their interpretation by providing an unbiased description of the material's structural and electronic properties.

However, a significant spread in the theoretical value of ε_{dir}^{biax} also exists in the results of DFT simulations. Looking at recent literature in this area, there is currently a spread of about 0.5% or more—values of 1.5% to over 2%[24–27] have been reported—which significantly reduces the effectiveness of these methods as a useful complement to experimental results. On the other hand, such a spread is not surprising when considering the different choices of approximations involved in such calculations. One crucial choice within a KS-DFT is the exchange-correlation (XC) functional which affects how many-body effects are approximated in the KS effective mean-field potential. The most common approximations for the XC functional are the local density approximation (LDA)[28,29] and the generalised gradient approximation (GGA).[30] Results in this paper show that in fact LDA and GGA lead substantially to the same results. Other choices are related

to the particular implementation of DFT. A popular implementation, adopted in this work, is to build the single particle wavefunctions from plane wave basis functions.[18] Within the plane-wave implementation of DFT, in order to make the calculations computationally viable, atomic pseudopotentials (PPs) replace the real ionic potentials such that the core electrons are not explicitly considered and the valence electrons are described by pseudowavefunctions with fewer nodes,[16,31–34] which decreases the computational cost.[35]

A host of alternative pseudization techniques exist, and the interrelated choices of PP generation method, the description of the core-valence interaction, and the desired electronic configuration following the pseudization process (i.e. the remaining "pseudovalence"), all have significant effects on the DFT ground state and hence the resulting GW correction can also clearly be influenced by these choices. Establishing meaningful comparisons between results reported for methods such as DFT+GW can therefore often be difficult, as many applications of this technique rely on pseudopotentials to establish a ground state starting point. In this paper, we investigate the extent to which these choices affect the calculation of the quasiparticle gaps of pure Ge, and how these effects in turn translate to differences in the predictions of the strain induced transition from an indirect to direct quasiparticle band gap of Ge. The effect of the PP on the accuracy of GW was recently analyzed and discussed for ZnO in Ref. 36.[37] Here, we use plane wave based PP DFT calculations to investigate the effect of PP and other approximations on the GW correction for Ge.

After a short review of the computational methods (Sec. II), we calculate the GW corrected gaps of relaxed bulk Ge (Sec. III A) in order to test a range of popular norm-conserving PPs[31–34] which have often been applied to bulk Ge.[6,26,27,38–40] Systematic investigations are carried out to test the range of variation of the gaps as a function of the PP generation technique, level of DFT approximation, pseudovalence configuration, and interaction of the outer 4th shell electrons with the (semi-)core 3rd shell. The latter are investigated by studying and comparing 4-valence PPs (Ge^{4+}) with different unoccupied orbitals remaining in the PP configuration following pseudization, with and without the popular nonlinear core correction of Louie Froyen and Cohen,[41] and contrasting these with PPs which explicitly include the $3s^2 3p^6 3d^{10}$ electrons (Ge^{22+}) in the PP valence.

It is found that the range of variations of the satellite valleys of Ge due to different PP generation techniques are significant and comparable to the variations from alternative approximations to the exchange-correlation (XC) functional, different choices of the PP valence configuration, as well different descriptions of the core-valence interaction. This has important consequences for the next study presented in this paper, which investigates the reordering of satellite valleys as a function of hydrostatic and biaxial strain (Sec. III B). It is found that the value of ε_{dir} for biaxial and hydrostatic strain ($\varepsilon_{dir}^{hydro}$), extracted from quasiparticle gaps, can vary by about 0.4% as a function of the PP. Also, the fact that the elastic strain dependence of band gaps exhibits only a small difference between certain PPs is anticipated[38,42,43] and significant for understanding the variation in ε_{dir}. This indicates that the discrepancy in the band gap transition strains is mainly caused by the difference in the quasiparticle satellite valley positions calculated at zero pressure. The causes for the difference in these quasiparticle levels is thus investigated by analyzing the contribution to the self-energy corrections and the relative contribution of atomic states at the band edges.

II. METHODS

Properties of solid state systems derived from the total energy, which involves only occupied states, are often described to satisfactory accuracy within DFT.[18] On the other hand, DFT band gaps are systematically underestimated as a result of the derivative discontinuity of the exchange-correlation (XC) energy functional $E_{\rm xc}$ upon addition or removal of an electron.[20–22] This justifies the so-called DFT+GW approach where total energies, forces, and stresses are minimized within DFT to obtain a relaxed atomic configuration for the bulk material, while the quasiparticle levels $E^{\rm QP}_{n\mathbf{k}}$ (the indexes n and $\mathbf{k}$ indicate the band and the crystal momentum respectively) are obtained by correcting perturbatively the KS eigenvalues $\epsilon^{\rm KS}_{n\mathbf{k}}$ within the GW approach:

$$E^{\rm QP}_{n\mathbf{k}} = \epsilon^{\rm KS}_{n\mathbf{k}} + \langle \psi_{n\mathbf{k}} | \Sigma(E) - V_{\rm xc} | \psi_{n\mathbf{k}} \rangle. \qquad (1)$$

In Eq. 1, the XC potential is $V_{\rm xc} = \delta E_{\rm xc}/\delta\rho$ where ρ is the density and $E_{\rm xc}$ is the XC energy functional. The energy-dependent self-energy $\Sigma(E)$ is obtained from a convolution of the Green's function G and the dynamically screened Coulomb interaction W (hence GW). G and W are both calculated from KS wavefunctions $\psi_{n\mathbf{k}}$.

Pseudopotential plane wave DFT calculations are performed using the Quantum Espresso (QE) software package.[44] Subsequent GW corrections to the DFT band gap are performed using the YAMBO code.[45] All geometry relaxations are performed using a 12×12×12 Monkhorst-Pack (MP)[46] k-point mesh to a force tolerance of less than 10^{-4} Rydberg/bohr per unit cell, resulting in highly converged crystal structures. Subsequent DFT single-point calculations using 8x8x8 MP k-points with a large number of unoccupied states are performed at the relaxed geometries to obtain the KS wavefunctions used to calculate G and W. Reducing the density of k-points from 12×12×12 to 8×8×8 results in significant savings in computational load at the DFT and GW steps and very little (3–4 meV or less) change in the quasiparticle gaps. 40 Rydberg kinetic cutoff E_{cut} of the plane wave basis set is used for all Ge^{4+} PPs, which achieves convergence of the total stress per unit cell to less than

10^{-4} Rydberg/Bohr^3. A much larger value of $E_{cut} = 260$ Rydberg is needed for Ge^{22+} to achieve the same level of convergence.

Based on the results presented in Table I, two norm-conserving LDA PPs are selected to calculate the high-symmetry satellite valleys of bulk Ge under hydrostatic and (100) biaxial strain within the DFT+GW approach. This involves relaxing the crystal structure for a given Ge PP within DFT, and subsequently introducing strain relative to the relaxed structure. The latter involves fixing the (100) bulk lattice constants ($a_{\rm lat}$) to equally strained values for hydrostatic strain, or straining $a_{lat,100}$ and $a_{lat,010}$ while allowing $a_{lat,001}$ to relax for biaxial strain.

GW corrections to the KS eigenvalues are calculated at the highest occupied state at Γ, and lowest unoccupied states at Γ, L, X, and the X valley which lies at ∼85% of the Γ−X k-path in the Ge Brillouin Zone (BZ). In all GW calculations, the size of the dielectric response matrix $\epsilon_{\mathbf{G},\mathbf{G'}}$ is converged to better than 5 meV change in the quasiparticle gaps per increase of 1 Ha in the energy cutoff (proportional to the number of off-diagonal elements of $\epsilon_{\mathbf{G},\mathbf{G'}}$). The number of unoccupied states is also increased until the change in the quasiparticle gaps is less than 5 meV per increase of 100 unoccupied states. We find that including 496 unoccupied states in G and W consistently achieves this level of accuracy for all Ge^{4+} PPs, while 978 unoccupied states are needed for the Ge^{22+} PP (see Table I).

We employ norm-conserving,[47] separable[48] pseudopotentials, which are available from the QE website[49] and the Theory and Simulation of Materials (THEOS) website.[50] These include Bachelet-Hamann-Schlüter (BHS),[31,32] Troullier-Martins (TM),[33] Goedecker-Teter-Hutter (GTH),[?] GTH1996 We also generate PPs using the ONCV code[51] and the Atomic Pseudopotentials Engine (APE).[52] In section III.A the Ge^{4+} PP valence is used to compare a range of popular norm-conserving pseudization approaches[31–34,51] and XC functionals at zero pressure. The effect of an approximate description of the core-valence interaction by comparing pseudopotentials generated with and without a nonlinear core correction (NLCC)[41] is also studied. The method in Ref. 53 is then selected to test the effect of the inclusion of the electrons from the second outer most shell, such that interactions between valence and semicore electrons are included explicitly.

Results are compared to previous[39,54,55] DFT+GW; in all of these previous works the lattice constant was fixed to the experimental value, which can facilitate comparisons of band gaps between methodologies due to the sensitivity of the gaps to crystal structure. However, calculating bandstructures at fixed lattice constant has a deleterious effect on investigations involving strain, as the equilibrium geometry is not obtained in that case. To allow for consistent comparisons with results in the literature, we calculate band gaps for relaxed structures as well as for cases in which $a_{\rm lat}$ is fixed to experiment. This also provides an initial rough estimate of the sensitivity of energy gaps to hydrostatic strain.

III. RESULTS

A. Zero pressure quasiparticle gaps

Focusing first on the band gaps obtained for relaxed Ge, the results are summarized in Table I. The first observation to make is the very wide spread of GW results within a typical set of DFT and PP approximations. Depending on the combination of the PP generation method, XC functional and description of the pseudovalence, band gaps at relaxed geometries can vary widely; we observe a maximum variation of the 1.53 eV, 0.70 eV, and 0.53 eV for the Γ, L and X valleys obtained at relaxed $a_{\rm lat}$.

1. *Comparison with the experiment.*

We start by comparing the results obtained at the relaxed geometry $a^0_{\rm lat}$ (i.e. minimum energy atomic configurations) with the experiment.

a. XC functional: When no NLCC is included (see below), the corrected LDA energy gaps of the valleys are generally in qualitative and in few cases even in good quantitative agreement with the experiment. On the other hand, the corrected GGA[30] energy gaps are largely underestimated and Ge is predicted to be a direct gap semiconductor or even a semimetal. The difference of performance is mostly due to the differences in the DFT electronic structure, though also the GW corrections for the GGA are systematically smaller (by about 80–180 meV).

b. PP method: We find that both PP 1 (TM) and PP 2 (GTH) gives a good quantitative agreement with gaps within 10–15% the experimental value and predicting the correct valley ordering.

c. NLCC: As it has been shown previously,[55] the inclusion of the usual NLCC[41] to account for core-valence interaction does not necessarily improve the bandstructure of Ge with respect to experiment.[2] In fact, the following trend can be observed: for all entries which include NLCC (PP 6–9), zero pressure energy gaps at the satellite valleys are out of order relative to experiment and significantly lower relative to comparable entries (similar PP method and $V_{\rm xc}$, see PP 1–5) which do not include NLCC. This trend also holds when comparing with the LDA PP calculation of Shirley *et al.*[55] It is interesting to note that when comparing the Ge^{4+} LDA PPs (PP 1–3 compared to PP 6 and 8) at zero pressure, the GW corrections are consistently smaller, typically by 50–100 meV, for PPs which incorporate the NLCC. However, we need to stress that we do not treat consistently the NLCC in the GW framework: in Eq. 1 the $V_{\rm xc}$ is evaluated at the valence density rather than at the total density (including the model core density), which is used

TABLE I. Energy gaps of the Γ, L and ∼0.85X (minimum along Γ−X k-path) valleys, and the gap at the X point, relative to the VBM at Γ, calculated from DFT+GW. Values in brackets denote the magnitude of the GW correction relative to the DFT gap. For results from the literature, the GW correction is included only where available. Underlined values indicate L gaps which correspond to the minimum gap. Units of energy gaps and corrections are in eV. Columns 2–4 signify the PP generation method, XC functional, and the pseudovalence electronic configuration (PP 1–9 correspond to Ge^{4+}, and PP 10 to Ge^{22+}). Column 5 denotes whether a nonlinear core correction (NLCC) is present. PPs used for calculations performed in this work are labelled 1 to 10. PPs 1–4 were obtained from the QE distribution,[44,49] PPs 5–7 from THEOS,[50] PPs 8 and 9 were generated using the ONCVPSP code,[51] and PP 10 was generated using the APE code.[52]

PP label	Method	V_{xc}	config.	NLCC	a_{lat} (Å)	Γ	L	X_{min}	X
1	TM	LDA	$4s^2 4p^2 4d^0 4f^0$	no	5.57	0.87 (0.59)	<u>0.76</u> (0.53)	0.96 (0.51)	1.15 (0.51)
					5.66[a]	0.37 (0.51)	0.56 (0.48)	0.98 (0.47)	1.17 (0.47)
2	GTH	LDA	$4s^2 4p^2 4d^0$	no	5.57	1.01 (0.64)	<u>0.84</u> (0.56)	1.00 (0.53)	1.19 (0.53)
					5.66[a]	0.50 (0.56)	0.63 (0.50)	1.01 (0.58)	1.24 (0.52)
3	BHS	LDA	$4s^2 4p^2$	no	5.62	1.30 (0.55)	<u>0.98</u> (0.52)	1.05 (0.52)	1.24 (0.53)
					5.66[a]	0.99 (0.51)	<u>0.86</u> (0.49)	1.05 (0.49)	1.24 (0.50)
4	TM	GGA	$4s^2 4p^2 4d^0 4f^0$	no	5.77	-0.12 (0.41)	0.27 (0.31)	0.86 (0.23)	1.00 (0.16)
					5.66[a]	0.49 (0.50)	0.52 (0.39)	0.82 (0.30)	1.00 (0.30)
5	GTH	GGA	$4s^2 4p^2 4d^0$	no	5.75	0.19 (0.56)	0.46 (0.42)	0.90 (0.30)	1.09 (0.39)
					5.66[a]	0.70 (0.62)	<u>0.64</u> (0.45)	0.86 (0.33)	1.05 (0.26)
6	TM	LDA	$4s^2 4p^2$	yes	5.70	0.41 (0.49)	0.54 (0.44)	0.91 (0.41)	1.09 (0.42)
					5.66[a]	0.69 (0.54)	<u>0.65</u> (0.48)	0.90 (0.45)	1.09 (0.45)
7	TM	GGA	$4s^2 4p^2$	yes	5.86	-0.22 (0.41)	0.27 (0.28)	0.92 (0.20)	1.03 (0.16)
					5.66[a]	0.93 (0.57)	<u>0.72</u> (0.42)	0.85 (0.31)	1.03 (0.30)
8	ONCV	LDA	$4s^2 4p^2$	yes	5.63	0.56 (0.54)	0.61 (0.49)	0.91 (0.47)	1.10 (0.48)
					5.66[a]	0.37 (0.51)	0.53 (0.47)	0.92 (0.45)	1.11 (0.46)
9	ONCV	GGA	$4s^2 4p^2$	yes	5.76	0.11 (0.53)	0.43 (0.40)	0.91 (0.30)	1.10 (0.30)
					5.66[a]	0.67 (0.60)	<u>0.63</u> (0.44)	0.81 (0.32)	1.06 (0.32)
10	TM	LDA	$3s^2 3p^6 3d^{10} 4s^2 4p^2$	no	5.66	0.54 (0.80)	<u>0.51</u> (0.53)	0.73 (0.34)	0.94 (0.30)
11[c]	HSC[d]	LDA	$4s^2 4p^2$	yes	5.66[a]	0.53 (0.62)	0.70 (0.69)		1.28 (0.78)
12[c]	CPP[b]	HF	$4s^2 4p^2$	N/A	5.66[a]	0.85	<u>0.73</u>		1.09
13[e]	BHS	LDA	$3s^2 3p^6 3d^{10} 4s^2 4p^2$	no	5.66[a]	0.81	<u>0.71</u>		
14[f]	Kerker[g]	LDA	$3s^2 3p^6 3d^{10} 4s^2 4p^2$	no	5.66[a]	0.85 (1.11)	<u>0.65</u> (0.69)		0.98 (0.42)
AE[h]		LDA			5.66[a]	0.89 (0.97)	<u>0.57</u>		
AE[i]		LDA				1.11 (1.31)	0.51 (0.16)		0.49 (-0.17)
Experiment[2]					5.66	0.90	0.74		1.16

[a] Lattice constant a_{lat} fixed to experimental value,[2] a_{lat} is relaxed in all other cases. For PP 10, the relaxed a_{lat} equals the experimental value.

[b] Correction due to core-valence interaction is provided by the core-polarization-potential,[55] derived from the interaction of valence electrons with induced core dipoles. This approach accounts for the core-valence correlation via a dynamical screening term which is used to construct the GW correction, core-valence exchange is treated within Hartree-Fock theory.[55]

[c] Shirley *et al.*[55,56]

[d] Norm-conserving Hamann-Schlüter-Chiang PP.[47]

[e] Rohlfing *et al.*[39]

[f] Tiago *et al.*[54]

[g] The Kerker PP generation method[57] was used here.[54]

[h] Full potential, all electron (AE) calculations of Kotani and Schlifgaarde.[58] Corrections due to spin-orbit interactions are not included for comparison.

[i] Full potential, all electron (AE) calculations of Ku and Eguiluz with a non-selfconsistent GW correction.[59] a_{lat} not specified in Ref. 59.

to determine the DFT eigenenergies and eigenfunction. This introduces an error that may explain the poor performance of the PP with NLCC. Preliminary results[60] in which the NLCC to the V_{xc} were taken into account in Eq. 1 show that indeed the corrections are larger than that presented in Table I, and in particular too large. Furthermore, the order and relative energy of the satellites valleys is completely wrong. This seems to suggest that the core contributions need to be accounted for both in the self-energy Σ and XC potential V_{xc}, as there is a partial cancellation of errors (see discussion below for the PP with semicore electrons). Hence, the apparent trend in results shown here are not necessarily indicative of a weakness in the NLCC which leads to a smaller GW correction to the gap.

d. Semicore electrons: The effect of core-valence partitioning and the role of semicore electrons have been previously studied for a range of compound

TABLE II. Variations of energy gaps of the Γ, L and X (minimum along the Γ−X k-path) valleys relative to the VBM at Γ, calculated from DFT+GW when calculated at the relaxed lattice constant $a_{\rm lat}^0$ rather than at the experimental lattice constant $a_{\rm lat}^{\rm exp}$. The first column reports the PP (numbering as in Table I), the second reports $\Delta a_{\rm lat} = a_{\rm lat}^{\rm exp} - a_{\rm lat}^0$; columns 3–5 report the variations with the lattice constant of the energy gaps at Γ, L and $X_{\rm min}$ (minimum along the Γ−X k-path) relative to the VBM with in parenthesis the variation of the GW correction.

PP	$\Delta a_{\rm lat}$	Γ	L	$X_{\rm min}$
			LDA+GW	
1	−0.09	0.50(0.08)	0.20(0.05)	−0.02(0.04)
2	−0.09	0.51(0.08)	0.21(0.06)	−0.01(0.05)
3	−0.04	0.31(0.04)	0.12(0.03)	0.00(0.03)
6	+0.04	−0.28(−0.05)	−0.11(−0.04)	0.01(−0.04)
8	−0.03	0.19(0.03)	0.08(0.02)	−0.01(0.02)
			PBE+GW	
4	0.11	−0.61(−0.09)	−0.25(−0.08)	0.04(−0.07)
5	0.09	−0.51(−0.06)	−0.18(−0.03)	0.04(−0.03)
7	0.20	−1.15(−0.16)	−0.45(−0.14)	0.07(−0.11)
9	0.10	−0.56(−0.07)	−0.20(−0.04)	0.10(−0.02)

semiconductors,[61,62] and for Ge.[39,54] When including explicitly the semicore electrons, we obtain the correct order for Γ, L, and X valleys (PP 10) once the GW correction is applied—in qualitative agreement with previous calculations[39,54,58]—although in all cases involving Ge^{22+}, satellite valleys are underestimated compared to experiment. It is also noted that at the LDA level, the energy gaps are in agreement with all electron results. In particular, Ge is predicted to be a semimetal, e.g. it has a negative energy gap at Γ of −0.26 eV, which agrees exactly with the full potential calculations of Shirley *et al.*[56] Also, for the direct Γ gap, reasonable agreement with the all electron calculations of Ku and Eguiluz (who reported −0.20 eV) is obtained at the LDA level.[59] Then, though the corrected band gap at Γ is smaller than in the experiment, the GW correction is the significantly larger than those obtained without semicores.

2. *Effect of the lattice constant*

In Table II we analyze the impact of calculating the GW gaps at either the experimental lattice constant $a_{\rm lat}^{\rm exp}$ or at the relaxed geometry $a_{\rm lat}^0$. Since $a_{\rm lat}^0$ is influenced by the choice of the XC functional we group the results depending on the level of approximation: the LDA tends to underestimate the lattice constant (with the exception of PP 6), whereas the GGA tends to overestimate it. Then, at the experimental lattice constant, the band gaps are effectively calculated under tensile strain for the LDA (except PP 6) and under compressive strain for the GGA (and the PP 6). As a consequence of the band gap pressure dependence, for the LDA (again excluding the PP 6), the band gaps Γ − Γ and Γ−L are consistently smaller at $a_{\rm lat}^{\rm exp}$ than at $a_{\rm lat}^0$ and, with the exception of PP 3, the fundamental gap is direct at Γ. Conversely, for the GGA (and the PP 6), the band gaps Γ−Γ and Γ−L are consistently larger at $a_{\rm lat}^{\rm exp}$ than at $a_{\rm lat}^0$ and, with the exception of PP 4, the fundamental gap is indirect (Γ−L). The largest contribution to these differences comes clearly from the difference in the DFT band gaps: the contribution from the GW correction is about 6–8 times smaller for Γ − Γ and about 3–4 times smaller for Γ−L. The overall effect of the GW correction is then to increase—in relative terms—the pressure dependence coefficient of the Γ − Γ gap with respect to the Γ−L gap. The band gap Γ−$X_{\rm min}$ has an opposite and much weaker dependence of the pressure than Γ − Γ and Γ−L. The effect of the GW correction in this case is relatively large and has opposite sign with respect to the overall difference, meaning that the GW correction weakens the pressure dependence with respect to the DFT results for the Γ−$X_{\rm min}$ band gap.

The PP method affects $a_{\rm lat}^0$ as well. Specifically, for the LDA, the difference $a_{\rm lat}^0 - a_{\rm lat}^{\rm exp}$ ranges between −0.09 Å and +0.04 Å whereas for the GGA ranges between 0.09 Å and 0.20 Å. Regarding the calculated pressure dependence, PP 1, PP 2, PP 4, PP 5, PP 7, and PP 9 give values between 15.28 meV/kbar and 17.33 meV/kbar for Γ − Γ, and between 5.72 meV/kbar and 6.78 meV/kbar for Γ−L, in reasonable agreement with the experimental values (see Table III), although slightly overestimated. On the other hand, the agreement with experiment is worse for PP 3, PP 6 and PP 8, which largely overestimate the experimental values.

To summarise, due to the strong pressure dependence of the electronic structure, the results change drastically when considering either $a_{\rm lat}^{\rm exp}$ or $a_{\rm lat}^0$. In particular, results for the band gap at Γ can vary as much as by 1.15 eV (PP 7) and consequently the system can change from a semimetal to an indirect band gap semiconductor. Here we use the values at $a_{\rm lat}^{\rm exp}$ only to facilitate the comparison of the results, while results at $a_{\rm lat}^0$ are used as reference for the calculations under tensile strain.

TABLE III. Hydrostatic pressure coefficients of quasiparticle conduction band valleys in Ge, obtained from DFT+GW calculations on PP 1 and PP 2. Values in parenthesis correspond to uncorrected DFT energies. The pressure per unit cell (in kbar) is extracted for each value of strain and the quasiparticle levels are fitted to a line. Units are in meV/kbar.

	Γ_c	L_c
PP 1	16.00 (15.61)	6.25 (5.99)
PP 2	16.09 (15.87)	6.57 (6.05)
Exp	15.3±0.5[63]	5.00[64]

3. Analysis of the results at a_{lat}^{exp}

In order to elucidate the impact of the PP generation method and how this compares to variations due to differing XC functionals, comparisons at fixed $a_{\rm lat}$ can be made between different PP methods which utilize the same $V_{\rm xc}$, and between different forms of $V_{\rm xc}$ for a given PP method. This is shown in Table IV. Here, comparisons are made by fixing one choice of approximation (where possible) and observing the resulting change in the high symmetry quasiparticle gaps as the other approximations are altered. In our classification, we neglect the difference in the LDA correlation of PW-LDA and PZ-LDA.[29] Hence PPs generated using PZ-LDA and PW-LDA are categorized under the same functional in Table I, II and IV.

a. XC functional: Variations of the gaps due to the choice of XC functional typically fall within the range of $0.2-0.3$ eV (Γ) and $0.05-0.1$ eV (L and X). As discussed in Sec. III A 2, at the experimental lattice constant the LDA is under tensile strain, while the GGA under compressive strain and as a consequence the energy gaps at Γ and L relative to the VBM are significantly larger within the GGA (this trend is reversed when the energy gaps at the relaxed geometry are considered).

b. NLCC and semicore electrons: Due to the inclusion of the NLCC (which as discussed in Sec. III A 1 are not considered in the *GW* corrections), the energy gap at Γ varies between $0.3-0.5$ eV while it stays within 0.2 eV for L and X. To note that, since the lattice constant $a_{\rm lat}^0$ predicted with the inclusion of NLCC is larger than without, at $a_{\rm lat}^{\rm exp}$ the PP with NLCC are in a better agreement with the experiment than without NLCC, in contrast to what observed at $a_{\rm lat}^0$. Surprisingly, the explicit inclusion of semicore electrons (PP 10) agrees moderately well with the 4 electron TM LDA pseudopotential (PP 1), when $a_{\rm lat}$ is fixed to the experimental value for PP 1. However, one should note that this is the result of comparing different LDA band gaps with very different *GW* corrections (see Table I).

c. PP method: The largest variations are observed for the Γ point gap (up to 0.63 eV), while the X valley varies the least—typically remaining within 0.1 eV. This was expected since the conduction band at the Γ point has s character, with the s being atom-centered, meaning that it is the most sensitive to the core-valence treatment as argued in Ref. 65. Contrasting the BHS generated PP (PP 3, $4s^24p^2$) with TM (PP 1, $4s^24p^24d^04f^0$) or GTH (PP 2, $4s^24p^24d^0$) results in large variations for Γ and L, the sum of which exceeds that of the other comparisons. The GTH and TM Ge^{4+} PPs (PP 1 and PP 2) are in better agreement with each other, compared to the difference of PP 1 or PP 2 with PP 3, and this relatively better agreement holds to within $\sim$10 meV when the lattice constant is allowed to relax. This indicates the changes associated with BHS vs. GTH and BHS vs. TM are due to an accumulation of the effects of changing PP generation method and changing PP configuration (i.e. the inclusion of unoccupied $4d$ and $4f$ states); different PPs that include unoccupied states but differ in the generation method exhibit better agreement than PPs that differ in the generation method and the inclusion of unoccupied states (PP 3 having only occupied states), resulting in better agreement between PP 1 and PP 2.

TABLE IV. Absolute variations of energy gaps of the Γ, L and X (minimum along the $\Gamma-$X k-path) valleys relative to the VBM at Γ, calculated from DFT+*GW*. Comparisons are made for different PP generation methods at the same $V_{\rm xc}$, different $V_{\rm xc}$ used to generate the PP for the same generation method, similar PP methods with and without NLCC, and similar PP methods with and without semicore electrons. To facilitate comparisons between the various methods, all results are taken from calculations in which $a_{\rm lat}$ is fixed to the experimental value. All units are in eV.

	$\lvert\Delta\Gamma\rvert$	$\lvert\Delta$L$\rvert$	$\lvert\Delta X_{\rm min}\rvert$	Total
		fixed $V_{\rm xc}$		
LDA				
TM vs. GTH	0.13	0.07	0.03	0.23
GTH vs. BHS	0.49	0.23	0.04	0.76
BHS vs. TM	0.62	0.30	0.07	0.99
GGA				
TM vs. GTH	0.23	0.12	0.05	0.39
LDA[a]				
TM vs. ONCV	0.32	0.12	0.02	0.46
GGA[a]				
TM vs. ONCV	0.27	0.09	0.02	0.38
		fixed PP method		
GTH				
LDA vs. GGA	0.20	0.01	0.15	0.36
TM				
LDA vs. GGA	0.12	0.04	0.16	0.32
TM[a]				
LDA vs. GGA	0.24	0.07	0.05	0.37
ONCV[a]				
LDA vs. GGA	0.30	0.10	0.10	0.49
		effect of NLCC		
TM, LDA				
w/ vs. w/out	0.32	0.09	0.08	0.49
TM, PBE				
w/ vs. w/out	0.45	0.20	0.03	0.68
		effect of semicore		
TM, LDA				
$Ge4^+$ vs. $Ge22^+$	0.18	0.05	0.25	0.47

[a] NLCC included in both PPs for this comparison.

4. Choice of PP method for calculations with biaxial strain

It is noted that the equilibrium lattice constant of PP 10 coincides with the experimental value, and PP 10 also exhibits the correct ordering of the satellite energies, with an indirect Γ−L gap, at zero pressure. This highlights the importance of the $3s^2 3p^6 3d^{10}$ semicore shell for structural properties, and the correct order of L, Γ and X indicates that PP 10 would be a suitable choice to study the biaxial strain dependence of the quasiparticle gaps. However, an unreasonably large computational cost is required to obtain accurate, converged GW corrections for PP 10; the presence of semicore orbitals translates to the requirement of a much higher number of unoccupied states for numerical convergence. Also, the reduced symmetry of anisotropically strained unit cells results in the requirement of a larger number of k-points to sample the BZ, relative to unstrained (or isotropically strained) cells. Therefore, using PP 10 to study biaxial strain requires a very high computational cost.

Thus, in order to balance physically reasonable accuracy with reasonable computational expense, we select PP 1 and PP 2 to study the variation of the high symmetry quasiparticle gaps as a function of tensile hydrostatic and (100) biaxial strain. It is noted that PP 2 exhibits a valley near the X point that is slightly lower with respect to the VBM compared to the Γ valley, which is unrealistic for Ge at zero pressure. Nevertheless, PP 2 is used to provide a comparison with PP 1 as they both exhibit an indirect minimum gap at L at zero pressure. As is shown below, these PPs yield significant differences in the theoretical values of ε_{dir}^{biax} and $\varepsilon_{dir}^{hydro}$. Despite the small differences in the pressure dependencies of PP 1 and PP 2, the results below indicate that the discrepancies in ε_{dir}^{biax} and $\varepsilon_{dir}^{hydro}$ between the PPs are mostly accounted for by the differences in the zero pressure satellite valley energies obtained from each PP.

B. Tensile strained quasiparticle gaps

TABLE V. Matrix elements of the various terms in the self-energy corrections applied to KS conduction states at Γ and L. The exchange term ($\Sigma_x - V_{\rm xc}$), where Σ_x is HF exchange) is enhanced relative to the dynamic screening term (Σ_c) for PP 2. All units are in eV.

	$\epsilon_{n\mathbf{k}}^{\rm KS}$	$\Sigma_x - V_{\rm xc}$	Σ_c	$\Sigma - V_{xc}$	$E_{n\mathbf{k}}^{\rm QP}$
PP 1					
Γ_v	0.00	−0.61	0.05	−0.56	−0.56
Γ_c	0.29	2.67	−2.65	0.02	0.31
L_c	0.23	2.65	−2.68	-0.03	0.20
PP 2					
Γ_v	0.00	−0.61	0.05	-0.56	-0.56
Γ_c	0.38	2.76	−2.69	0.07	0.45
L_c	0.28	2.69	−2.69	0.00	0.28

FIG. 1.(a) and FIG. 1.(b) show the movement of the high symmetry valleys as a function of hydrostatic and biaxial strain obtained from DFT+GW calculations. Comparing both cases, 0.5-0.6% hydrostatic strain for PP 1 (LDA $V_{\rm xc}$, TM generation method) and 0.8-0.9% PP 2 (LDA $V_{\rm xc}$, GTH generation method) result in a direct band gap transition, with $\varepsilon_{dir}^{hydro}$ of PP 2 being in good agreement with standard deformation potential theory.[66]

In FIG. 1.(a) it can be seen that for the TM generated PP, biaxial strains greater than 1.5% result in a direct minimum band gap at the Γ point. The lowering of the Γ valley below the L valley is expected due to the larger hydrostatic deformation potential at Γ compared to L.[66,67] This value of ε_{dir}^{biax} is in agreement with previous studies which used a similar PP[26] and here we show the range of GW corrected Γ, L, and X quasiparticle band gaps over a 3% range of (100) biaxial strain. Comparing this with FIG. 1.(b), similar qualitative behaviour can be observed for results derived from the GTH generated PP, while the value of ε_{dir}^{biax} is again increased by about 0.4%.

FIG. 1.(a) and FIG. 1.(b) show that there is reasonable agreement between both PPs for the strain dependencies of the quasiparticle band gaps at Γ and L. For example, if one rigidly shifts the Γ and L lines of PP 1 for biaxial strain (right panel of FIG. 1.(a)) to reflect the zero strain Γ−L separation of PP 2 (0.17 eV) (thus keeping the slopes of PP 1 for the Γ and L gaps with respect to biaxial strain) then one finds a value of ε_{dir}^{biax} of 1.8%, in close agreement with the value obtained for PP 2. Similarly, shifting the PP 2 lines to reflect the zero strain Γ−L separation of PP 1 (0.11 eV), one obtains a ε_{dir}^{biax} of 1.4%, only slightly below the value obtained for PP 1. Thus, the major cause of the discrepancy in the predicted values of ε_{dir} is narrowed down to the differences in the zero pressure satellite valley positions.

Thus an investigation into the underlying causes of the difference in the calculated zero pressure quasiparticle gaps between these two pseudopotentials is undertaken, in order to explain the disagreement in the predicted ε_{dir}^{biax}. We first note that the majority of the difference in the Γ_c−L_c separation between the PPs is accounted for by the KS eigenvalues $\epsilon_{n\mathbf{k}}^{\rm KS}$. FIG. 2.(a) and FIG. 2.(b) show the atomic orbital projected bandstructures, calculated for both PPs near the relevant band edges under 0% strain, in which the orbital projected density of states gives a normalized weight for each band. In both cases, the conduction valley at the Γ point is strongly s-like while the valence band maximum is strongly p-like. In general, both PPs show heavy contributions from $4s$ and $4p$ states in the vicinity of the band edges. However, PP 2 exhibits a much larger contribution from the $4d$ orbital compared to PP 1 in this region of the bandstructure, particularly at the L valley. PP 2 also yields a larger separation in energy between the L and Γ valleys. As is explained below, these findings are related.

It is important to note that the self-energy contribution to quasiparticle energies can be decomposed into an exchange term Σ_x and a correlation term Σ_c.[45] Relative

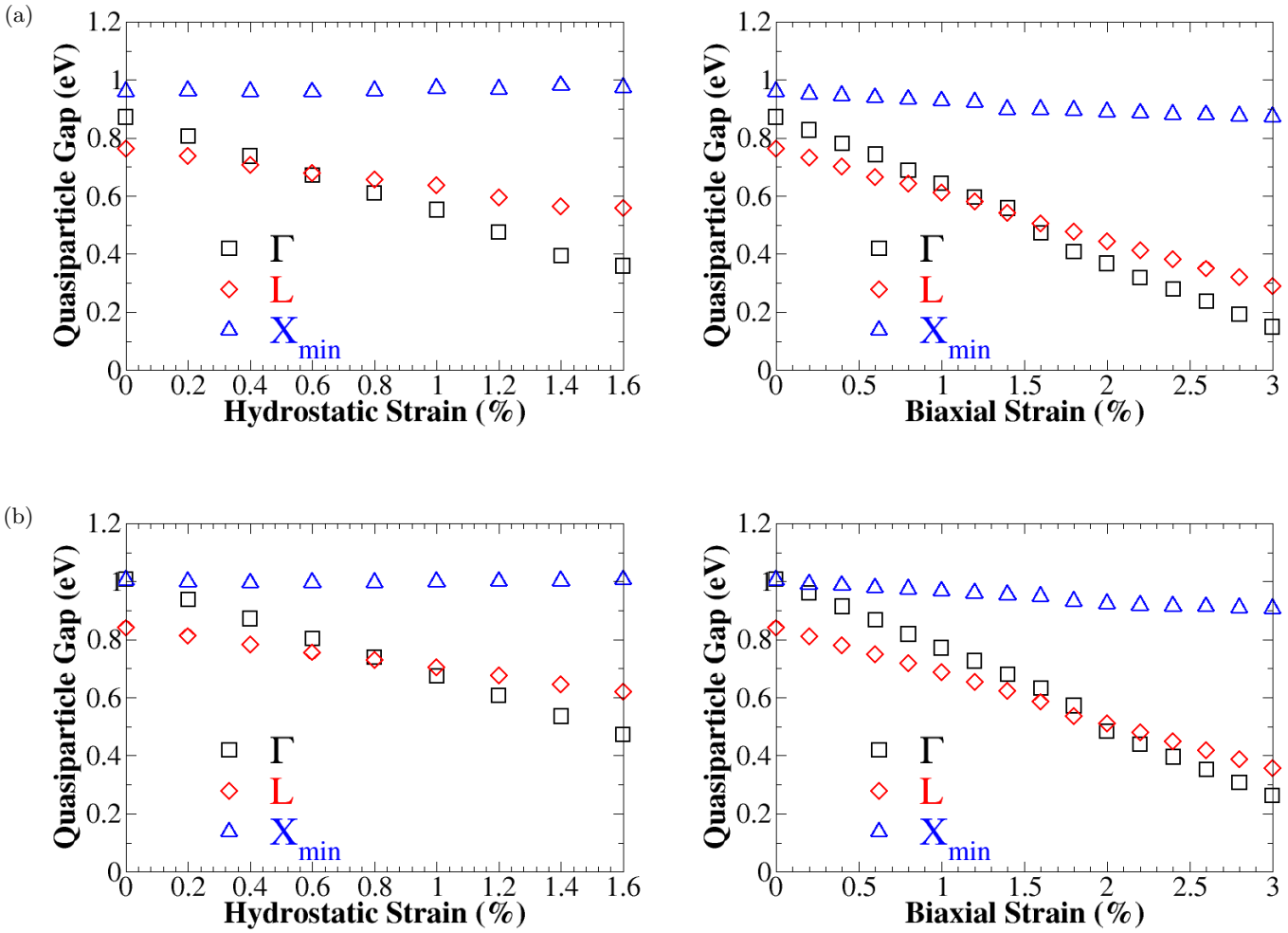

FIG. 1. (Top row) (a) shows quasiparticle gaps at Γ, L and ∼0.85(Γ−X) high symmetry satellite valleys calculated from DFT+GW for hydrostatic (left) and biaxial (right) tensile strain in bulk Ge, using PP 1 (Ge^{4+}, TM, LDA, no NLCC). (Bottom row) (b) shows quasiparticle gaps at Γ, L and ∼0.85(Γ−X) high symmetry satellite valleys calculated from DFT+GW for hydrostatic and biaxial tensile strain in bulk Ge, using PP 2 (Ge^{4+}, GTH, LDA, no NLCC).

to the DFT gap, the effect of Σ_x (i.e. the Hartree-Fock term or HF self-energy) is to increase the band gap to values above the experimental gap, while Σ_c decreases the gap relative to the HF gap, leading to good agreement with experimental band gaps for many semiconductors and insulators.[65] The relative contribution of Σ_x compared to Σ_c is thus a major factor in determining the magnitude of the resulting quasiparticle band gaps. To investigate this, we show the self-energy correction matrix elements for exchange and correlation at the valence and conduction band edges at L and Γ obtained for both PPs in Table V. It is observed that the PP 2 (with a greater $4d$-like character near the band edges—compare right panels of FIG. 2.(a) and FIG. 2.(b)) exhibits more positive self-energy corrections to the conduction band states, especially at the Γ point. This increases the separation between Γ_c and L_c by a larger amount for PP 2 compared to the Γ_c−L_c separation for PP 1. Also, for PP 2 the exchange contribution at L_c is large enough to cancel the contribution from dynamic correlation, which nullifies the net GW correction at L_c; the latter is negative for PP 1, so this also contributes to the result that the Γ_c−L_c separation is larger for PP 2. Bands involving the hybridization of atomic orbitals exhibit increased exchange terms if there is increased spatial overlap of the orbitals.[68–70] On the other hand, coincidence in energy would increase the magnitude of dynamic correlation.

Also note that covalent bonding in Ge occurs through s-p hybridization, with the occupied $4p$ orbital situated along the Ge-Ge bond (consistent with the valence band being strongly p-like),[71] and the $4s$ orbital centered on atomic sites. $4d$ orbitals, which are not strongly involved in bonding could also be localized, at least partially, near atomic sites. A larger $4d$ contribution at the relevant

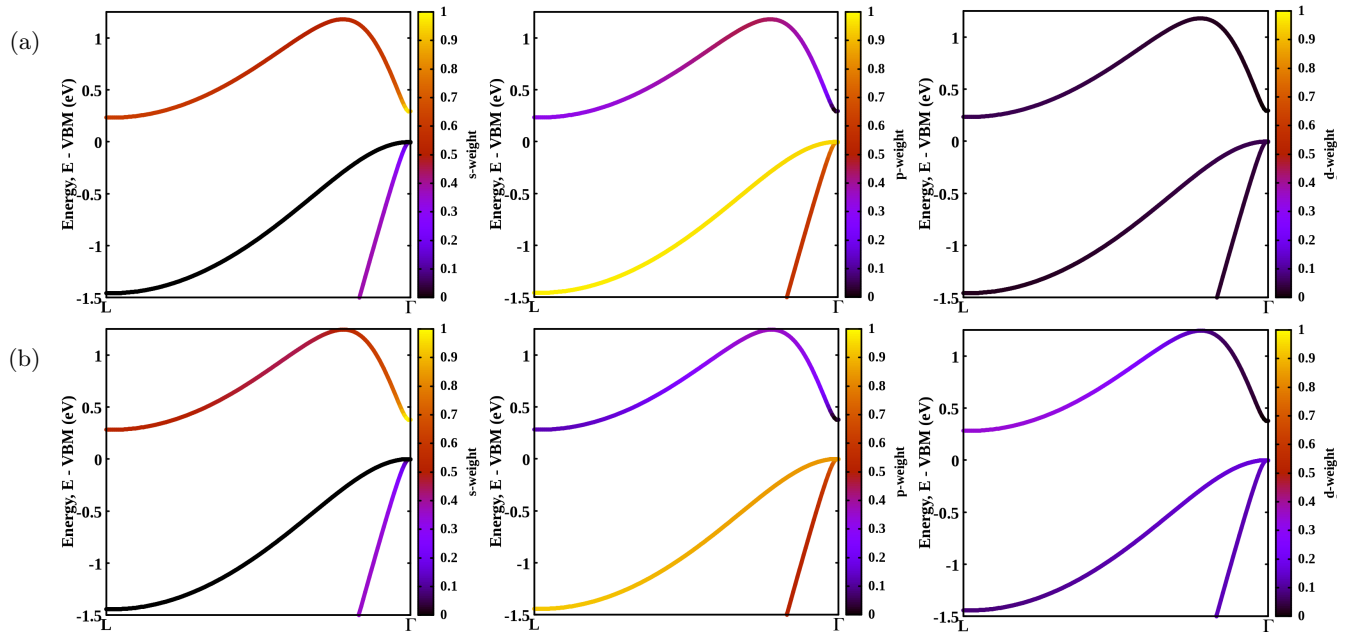

FIG. 2. (Top row) (a) Orbital projected DFT bandstructure of unstrained Ge along the L−Γ k-path for the s, p, and d states, plotted near the band edges, using PP 1 (TM, $4s^2 4p^2 4d^0 4f^0$). The f orbital has 0 weight in this region and is not shown. (Bottom row) (b) Orbital projected bandstructure of unstrained Ge along the L−Γ k-path for the s, p, and d states, plotted near the band edges, using PP 2 (GTH, $4s^2 4p^2 4d^0$). The band edges for PP 2 show a higher proportion of d states compared to PP 1, while the s and p weight is approximately similar for PP 1 and PP 2 in this region of the bandstructure.

band edges for PP 2 could lead to larger exchange interactions relative to PP 1, if the $4d$ and other orbitals associated with these bands share similar localization properties. As a preliminary test of the locality of the $4d$ states, we plotted the pseudowavefunctions of the 4th shell for the isolated pseudoatoms, and indeed find significant localization of the $4d$ orbitals near the atomic centre (not shown for brevity). This prompts a further investigation of the locality of the 4th shell orbitals in the bulk material.

To investigate the origin of the enhanced exchange energy, the 3-dimensional isosurfaces for densities ($|\psi_{n\mathbf{k}}(\mathbf{r})|^2$) corresponding to the relevant band edges are plotted near a Ge atom and shown for both PPs in FIG. 3.(a) and FIG. 3.(b). Clearly, the wavefunction of the L valley overlaps significantly in space with that of the Γ valley, for both PPs. Thus, for PP 2, the $4d$ orbital contributing to the L valley overlaps significantly with atom-centered $4s$ orbitals of the CB edge at Γ.

Interestingly, the exchange and correlation terms of the GW correction resulting from both PPs are very similar at the valence band edge Γ_v. This emphasises that it is the character of the conduction band states that is responsible for the discrepancy in the satellite valleys and ultimately the discrepancy in ε_{dir} as these PPs exhibit similar band gap pressure dependencies. Our analysis shows that there are enhanced positive exchange contributions at Γ_c and L_c for PP 2 compared to PP 1, as a result of the enhanced overlap between atomically localized states contributing to the band edges. This pushes the Γ_c valley of PP 2 up higher in energy compared to PP 1, and this results in the quasiparticle Γ_c−L_c separation being 60 meV greater for PP 2 compared to PP 1 at zero pressure.

The relative contributions of atomic states at band edges also plays an important role in determining the allowed optical transitions,[72] and thus has a major impact on the photoluminescence and absorption properties. The selection rules for optical transitions are determined by the change in orbital angular momentum between states involved in a transition, and thus on the symmetry properties of the corresponding bands. As (001) biaxially strained Ge is currently under investigation as an optically active material due to the onset of a direct minimum band gap,[6,8] it is important to investigate how the mixing of atomic-like orbitals at band edges is affected by biaxial strain. Under 0% strain, the direct $\Gamma_c - \Gamma_v$ transition involves a s-p change in orbital angular momentum l, which thus indicates an allowed optical transition for the direct Γ_c-Γ_v gap[72] as the associated transition matrix element does not couple states with the same symmetry and thus can be nonzero. Strong photoluminescence has been measured in biaxially strained Ge at low temperature,[9] suggesting that the Δl involved in the Γ point transition remains close to 1. To investigate this possibility, the orbital projected bandstructures for a range of strains are plotted along the L-Γ path. PP 1 is selected for this investigation as the enhanced proportion of $4d$ states at the top of the valence band for PP 2 is not realistic. The orbital projected bandstructures near the

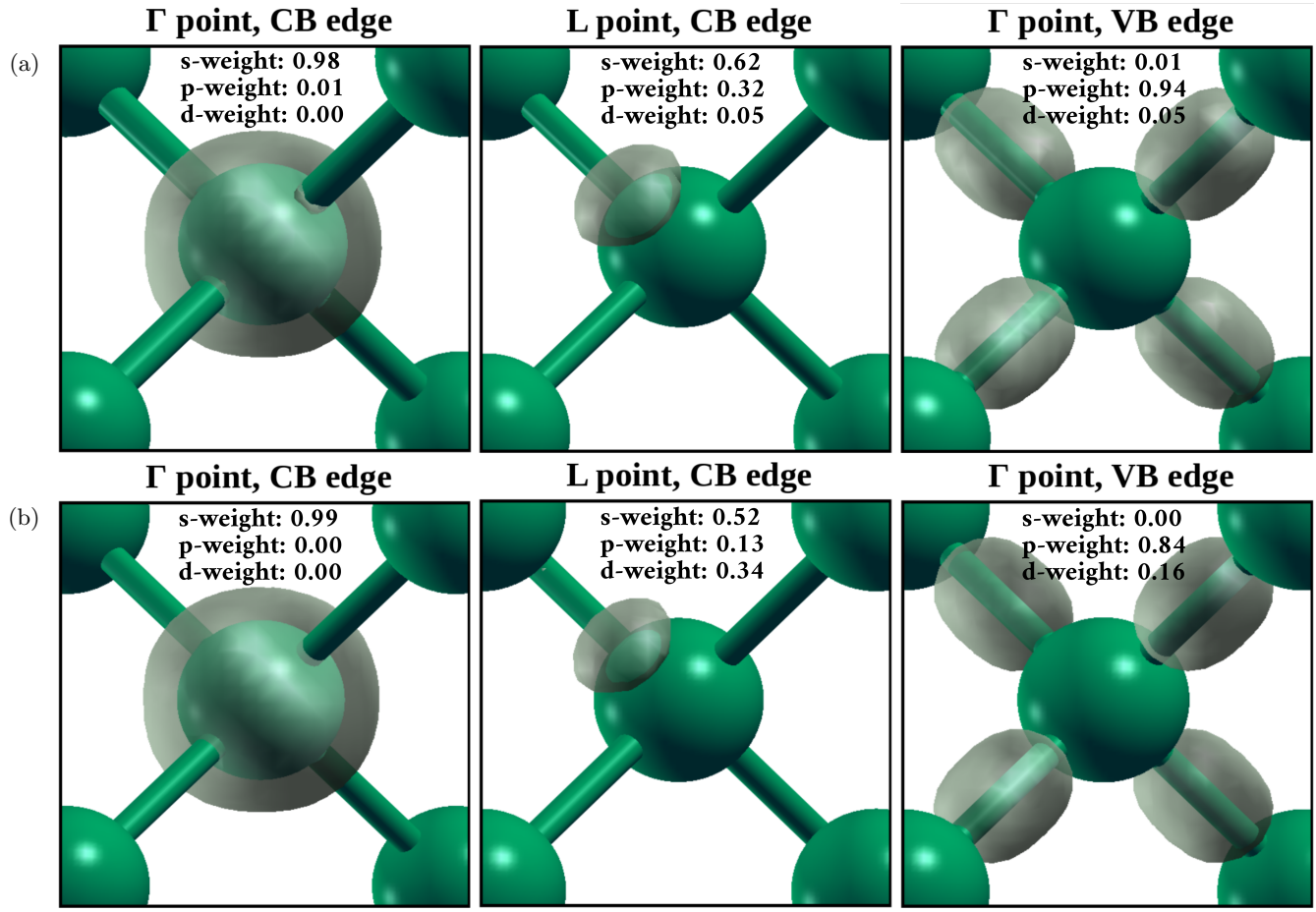

FIG. 3. Isosurfaces of a $|\psi_{n\mathbf{k}}(\mathbf{r})|^2$ for the band edges at Γ and L. Row (a) was obtained using PP 1, while row (b) was obtained using PP 2. The localization of the L-valley wavefunction to the atomic site shows that, for PP 2, the $4d$ orbitals at the L valley have significant overlap with the $4s$ states at the Γ valley.

conduction and valence band edges are shown in FIG. 4.(a) and FIG. 4.(b), respectively.

It can be seen from FIG. 3 that, as a function of tensile strain, the relative proportions of $4p$ states at Γ_v and $4s$ states at Γ_c do not significantly change. With large strain, as the band edges approach each other, a small transfer of $4s$ and $4p$ weight across the vertical Γ transition is observed, with the light hole (LH) taking up the change in orbital weight at the VBM. This may be a consequence of the bands edges (incorrectly) approaching degeneracy within DFT due to band gap underestimation. However, it is emphasised that even for highly strained Ge, Γ_v and Γ_c remain strongly p-like and strongly s-like, respectively, indicating a lack of suppression of optical transitions due to strain-induced orbital mixing.

IV. CONCLUSIONS

We presented the results of the DFT+GW approach applied to the calculation of the Γ, L, and X high symmetry gaps of the Ge bandstructure, using a range of different approximations. This work complements previous works in this area[6,24–27] with a systematic study of the influence of the choice of pseudization method, XC functional, and the level of approximation of the core-valence interaction on the Ge quasiparticle satellite valleys. Our investigations helped quantify the importance of these approximations on the indirect-direct band gap transition as a function of tensile strain.

Comparing the pressure coefficients extracted from DFT and GW corrected values, and in turn comparing these to previous theoretical and experimental studies shows the consistency of these methods in describing the linearity of the strain induced variation of the satellite valleys, despite the disagreement in the satellite valley separations. The predicted values of ε_{dir}^{biax} and $\varepsilon_{dir}^{hydro}$ thus disagree accordingly, such that the prediction of these transition strains primarily relies on an accurate assessment of the separation between the quasiparticle conduction band valleys at zero pressure.

This work shows that while inclusion of unoccupied orbitals in the pseudized electronic configuration has beneficial aspects, special attention should be paid to the

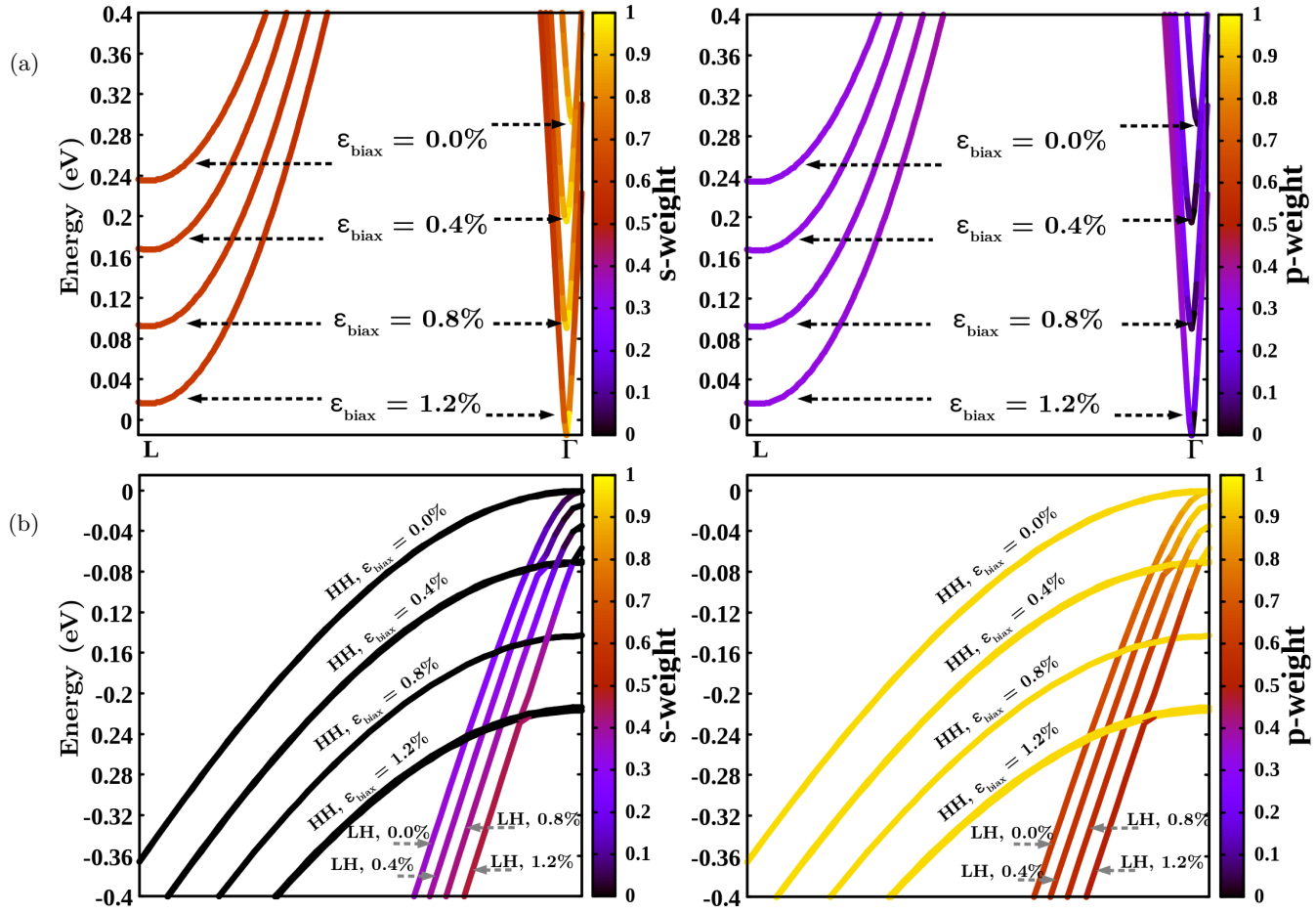

FIG. 4. (Top row) (a) shows the orbital projected DFT bandstructures of strained Ge along the Γ−L k-path for the s and p, plotted near the band edges, with the bands of increasing values of strain superimposed. PP 1 (TM, $4s^2 4p^2 4d^0 4f^0$) is used here. The f-orbital has 0 weight in this region and is not shown. For PP 1, the d orbital also has very low weight (see FIG. 2.(a) in this region, which does not change with strain, hence the d orbital is also omitted in this analysis. Four values of biaxial strain are shown for the conduction bands in the top row, and for the valence bands in the bottom row. Different scales for the k axis are used for the top and bottom rows; the valence bands are shown close to the BZ center for clarity. The 0 of the energy scales are set to the VBM of unstrained Ge. Note the transition to a direct minimum gap has already accrued for 1.2% biaxial strain, which is a consequence of using an uncorrected DFT bandstructure. Correcting the eigenvalues with the GW approximation increases the transition strain to 1.5%. As the light hole (LH) pushes up above the heavy hole (HH) with tensile strain, the weight of s and p orbitals along the LH band changes slightly with large strain. However, the relative weights of p orbitals at the VBM (light hole (LH) for tensile strained Ge) and s orbitals at the CBM remain quite similar for each value of biaxial strain.

resulting orbital hybridization in the conduction band. In particular, while the zero pressure quasiparticle satellite valleys, obtained from self-energy corrections to KS states, are correctly ordered in energy which (due to the reasonable pressure dependencies) leads to reasonable predictions of the strain induced direct to indirect band gap transition for both Ge^{4+} PPs, small differences in the arrangement of unoccupied pseudo-wavefunctions leads to significant differences in the prediction of ε_{dir} as obtained by the DFT+GW approach. Finally, by providing a breakdown of the contributions of atomic orbitals to the relevant band edges, we show that even for highly strained Ge, the vertical optical transition at Γ should not be suppressed by strain-induced orbital mixing.

ACKNOWLEDGMENTS

The authors acknowledge the use of computational facilities at the Atomistic Simulation Centre in Queen's University Belfast. This work is financially supported by the Department for the Employment of Northern Ireland and InvestNI through the US-Ireland R&D partnership programme (USI-073). The authors are indebted to Michael Clavel, Dzianis Saladukha, Tomasz J. Ochalski, Felipe Murphy-Armando, and Mantu K. Hudait for insightful discussions. The authors also appreciate helpful discussions with Brian Cunningham on self-consistent GW techniques and with Andrea Ferretti, An-

drea Marini, Ivan Marri and Davide Sangalli on the nonlinear core corrections to the pseudopotential. In particular, they thank Andrea Ferretti for providing the code which allowed to test the inclusion of the nonlinear core corrections into the equation for the quasiparticle energies.

DATA AVAILABILITY

All raw data is available upon request from the corresponding author.

* corresponding author: g.greene-diniz@qub.ac.uk

[1] F. Seitz and N. G. Einspruch, *Electronic Genie: The Tangled History of Silicon* (University of Illinois Press, 1998).
[2] O. Madelung, *Semiconductors: Data Handbook* (Springer Berlin Heidelberg, 2004).
[3] M. L. Lee, E. A. Fitzgerald, M. T. Bulsara, M. T. Currie, and A. Lochtefeld, Journal of Applied Physics **97**, 011101 (2005).
[4] M. Clavel, P. Goley, N. Jain, Y. Zhu, and M. K. Hudait, IEEE Journal of the Electron Devices Society **3**, 184 (2015).
[5] J. Michel and M. Romagnoli, *SPIE Newsroom*, (2012).
[6] N. Pavarelli, T. J. Ochalski, F. Murphy-Armando, Y. Huo, M. Schmidt, G. Huyet, and J. S. Harris, Phys. Rev. Lett. **110**, 177404 (2013).
[7] D. Liang and J. E. Bowers, Nature Photonics **4**, 511 (2010).
[8] D. Sabbagh, J. Schmidt, S. Winnerl, M. Helm, L. D. Gaspare, M. D. Seta, M. Virgilio, and M. Ortolani, ACS Photonics **3**, 403 (2016).
[9] J. R. Sánchez-Pérez, C. Boztug, F. Chen, F. F. Sudradjat, D. M. Paskiewicz, R. Jacobson, M. G. Lagally, and R. Paiella, Proceedings of the National Academy of Sciences **108**, 18893 (2011).
[10] M. V. Fischetti and S. E. Laux, J. Appl. Phys. **80**, 2234 (1996).
[11] J. Menéndez and J. Kouvetakis, Applied Physics Letters **85**, 1175 (2004).
[12] G. Pizzi, M. Virgilio, and G. Grosso, Nanotechnology **21**, 055202 (2010).
[13] C. Boztug, J. R. Sánchez-Pérez, F. F. Sudradjat, R. Jacobson, D. M. Paskiewicz, M. G. Lagally, and R. Paiella, Small **9**, 622 (2013).
[14] M. de Kersauson, M. Prost, A. Ghrib, M. El Kurdi, S. Sauvage, G. Beaudoin, L. Largeau, O. Mauguin, R. Jakomin, I. Sagnes, G. Ndong, M. Chaigneau, R. Ossikovski, and P. Boucaud, Journal of Applied Physics **113**, 183508 (2013).
[15] P. Hohenberg and W. Kohn, Phys. Rev. **136**, B864 (1964).
[16] M. L. Cohen, Physica Scripta **T1**, 5 (1982).
[17] M. C. Payne, M. P. Teter, D. C. Allan, T. A. Arias, and J. D. Joannopoulos, Rev. Mod. Phys. **64**, 1045 (1992).
[18] R. Martin, *Electronic Structure: Basic Theory and Practical Methods* (Cambridge University Press, 2004).
[19] W. Kohn and L. J. Sham, Phys. Rev. **140**, A1133 (1965).
[20] J. P. Perdew, R. G. Parr, M. Levy, and J. L. Balduz, Phys. Rev. Lett. **49**, 1691 (1982).
[21] L. J. Sham and M. Schlüter, Phys. Rev. B **32**, 3883 (1985).
[22] R. W. Godby, M. Schlüter, and L. J. Sham, Phys. Rev. B **37**, 10159 (1988).
[23] L. Hedin, Phys. Rev. **139**, A796 (1965).
[24] H. Tahini, A. Chroneos, R. W. Grimes, U. Schwingenschlgl, and A. Dimoulas, J. Phys: Condens. Matt. **24**, 195802 (2012).
[25] Y. Hoshina, K. Iwasaki, A. Yamada, and M. Konagai, Jap. J. Appl. Phys. **48**, 04C125 (2009).
[26] F. Murphy-Armando and S. Fahy, J. Appl. Phys. **109**, 113703 (2011).
[27] K. Sakata, B. Magyari-Kpe, S. Gupta, Y. Nishi, A. Blom, and P. Dekc, Comp. Mat. Sci. **112**, 263 (2016).
[28] J. P. Perdew and A. Zunger, Phys. Rev. B **23**, 5048 (1981).
[29] J. P. Perdew and Y. Wang, Phys. Rev. B **45**, 13244 (1992).
[30] J. P. Perdew, K. Burke, and M. Ernzerhof, Phys. Rev. Lett. **77**, 3865 (1996).
[31] G. B. Bachelet, D. R. Hamann, and M. Schlüter, Phys. Rev. B **26**, 4199 (1982).
[32] D. R. Hamann, Phys. Rev. B **40**, 2980 (1989).
[33] N. Troullier and J. L. Martins, Phys. Rev. B **43**, 1993 (1991).
[34] S. Goedecker, M. Teter, and J. Hutter, Phys. Rev. B **54**, 1703 (1996).
[35] Two constraints are imposed on the generation of pseudowavefunctions (i.e. the "pseudization"of the all-electron wavefunctions); i) they must match the true wavefunction outside of a cutoff radius, and (for norm-conserving PPs) ii) the normalization of the pseudowavefunctions is constrained to equal that of the true wavefunctions. The latter condition can be relaxed, as e.g. for the ultrasoft PPs. PP schemes that comply to the latter constraint are referred to as norm-conserving.
[36] H. Jiang and P. Blaha, Phys. Rev. B **93**, 115203 (2016).
[37] The authors of Ref. 36 investigated the effect of highly localised orbitals on the *GW* correction for calculations involving LAPW basis sets; the authors then compared these results to PP calculations which clarified some aspects of how the accuracy of *GW* calculations are affected by PPs, focusing primarily on ZnO, but also reporting bandgaps for other semiconductors (excluding Ge).
[38] K. Chang, S. Froyen, and M. L. Cohen, Solid State Communications **50**, 105 (1984).
[39] M. Rohlfing, P. Krüger, and J. Pollmann, Phys. Rev. B **57**, 6485 (1998).
[40] D. Rideau, M. Feraille, L. Ciampolini, M. Minondo, C. Tavernier, H. Jaouen, and A. Ghetti, Phys. Rev. B **74**, 195208 (2006).
[41] S. G. Louie, S. Froyen, and M. L. Cohen, Phys. Rev. B **26**, 1738 (1982).
[42] X. Zhu, S. Fahy, and S. G. Louie, Phys. Rev. B **39**, 7840 (1989).
[43] E. Ghahramani and J. E. Sipe, Phys. Rev. B **40**, 12516 (1989).
[44] P. Giannozzi, S. Baroni, N. Bonini, M. Calandra, R. Car, C. Cavazzoni, D. Ceresoli, G. L. Chiarotti, M. Cococcioni, I. Dabo, A. D. Corso, S. de Gironcoli, S. Fabris, G. Fratesi, R. Gebauer, U. Gerstmann, C. Gougoussis, A. Kokalj,

M. Lazzeri, L. Martin-Samos, N. Marzari, F. Mauri, R. Mazzarello, S. Paolini, A. Pasquarello, L. Paulatto, C. Sbraccia, S. Scandolo, G. Sclauzero, A. P. Seitsonen, A. Smogunov, P. Umari, and R. M. Wentzcovitch, Journal of Physics: Condensed Matter **21**, 395502 (2009).
[45] A. Marini, C. Hogan, M. Gruening, and D. Varsano, Computer Physics Communications **180**, 1392 (2009).
[46] H. J. Monkhorst and J. D. Pack, Phys. Rev. B **13**, 5188 (1976).
[47] D. R. Hamann, M. Schlüter, and C. Chiang, Phys. Rev. Lett. **43**, 1494 (1979).
[48] L. Kleinman and D. M. Bylander, Phys. Rev. Lett. **48**, 1425 (1982).
[49] `http://www.quantum-espresso.org/pseudopotentials/`.
[50] `http://theossrv1.epfl.ch/Main/Pseudopotentials`.
[51] D. R. Hamann, Phys. Rev. B **88**, 085117 (2013).
[52] M. J. Oliveira and F. Nogueira, Computer Physics Communications **178**, 524 (2008).
[53] C. L. Reis, J. M. Pacheco, and J. L. Martins, Phys. Rev. B **68**, 155111 (2003).
[54] M. L. Tiago, S. Ismail-Beigi, and S. G. Louie, Phys. Rev. B **69**, 125212 (2004).
[55] E. L. Shirley, X. Zhu, and S. G. Louie, Phys. Rev. Lett. **69**, 2955 (1992).
[56] E. L. Shirley, X. Zhu, and S. G. Louie, Phys. Rev. B **56**, 6648 (1997).
[57] G. P. Kerker, Journal of Physics C: Solid State Physics **13**, L189 (1980).
[58] T. Kotani and M. van Schilfgaarde, Solid State Communications **121**, 461 (2002).
[59] W. Ku and A. G. Eguiluz, Phys. Rev. Lett. **89**, 126401 (2002).
[60] Obtained by using a version of the code still in development.
[61] R. Gómez-Abal, X. Li, M. Scheffler, and C. Ambrosch-Draxl, Phys. Rev. Lett. **101**, 106404 (2008).
[62] X.-Z. Li, R. Gmez-Abal, H. Jiang, C. Ambrosch-Draxl, and M. Scheffler, New Journal of Physics **14**, 023006 (2012).
[63] B. Welber, M. Cardona, Y.-F. Tsay, and B. Bendow, Phys. Rev. B **15**, 875 (1977).
[64] W. Paul and D. Warschauer, *Solids Under Pressure*, McGraw-Hill series in materials science and engineering (McGraw-Hill, 1963).
[65] M. S. Hybertsen and S. G. Louie, Phys. Rev. B **34**, 5390 (1986).
[66] S. Chuang, *Physics of Photonic Devices*, Wiley Series in Pure and Applied Optics (John Wiley & Sons, 2009).
[67] C. Boztug, J. R. Sánchez-Pérez, F. Cavallo, M. G. Lagally, and R. Paiella, ACS Nano **8**, 3136 (2014).
[68] A. Szabo and N. Ostlund, *Modern Quantum Chemistry: Introduction to Advanced Electronic Structure Theory*, Dover Books on Chemistry (Dover Publications, 1989).
[69] W. Aulbur, L. Jösson, and J. W. Wilkins, in *Solid State Physics*, Vol. 54, edited by F. Seitz, D. Turnbull, and H. Ehrenreich (Academic, New York, 2000).
[70] M. Rohlfing, P. Krüger, and J. Pollmann, Phys. Rev. Lett. **75**, 3489 (1995).
[71] W. Harrison, *Electronic Structure and the Properties of Solids: The Physics of the Chemical Bond*, Dover Books on Physics (Dover Publications, 1989).
[72] P. YU and M. Cardona, *Fundamentals of Semiconductors: Physics and Materials Properties*, Graduate Texts in Physics (Springer Berlin Heidelberg, 2010).